Electrically controlled water permeation through graphene oxide membranes

Electrically controlled water permeation through graphene oxide membranes

K.-G. Zhou[1,2*], K. S. Vasu[1,2*], C. T. Cherian[1,2], M. Neek-Amal[3,4], J. C. Zhang[5], H. Ghorbanfekr-Kalashami[4], K. Huang[1,2], O. P. Marshall[6], V. G. Kravets[6], J. Abraham[1,2], Y. Su[1,2], A. N. Grigorenko[6], A. Pratt[5], A. K. Geim[6], F. M. Peeters[4], K. S. Novoselov[6], R. R. Nair[1,2*]

[1]National Graphene Institute, University of Manchester, Manchester, M13 9PL, UK.

[2]School of Chemical Engineering and Analytical Science, University of Manchester, Manchester, M13 9PL, UK.

[3]Department of Physics, Shahid Rajaee Teacher Training University, 16875-163, Lavizan, Tehran, Iran.

[4]Department of Physics, University of Antwerpen, Groenenborgerlaan 171, B-2020 Antwerpen, Belgium.

[5]Department of Physics, University of York, York, YO10 5DD, UK.

[6]School of Physics and Astronomy, University of Manchester, Manchester M13 9PL, UK.

*kai-ge.zhou@manchester.ac.uk, vasusiddeswara.kalangi@manchester.ac.uk, rahul@manchester.ac.uk

Controlled transportation of water molecules through membranes and capillaries is of crucial importance in various areas of research from water purification to healthcare technologies[1-7]. Previous attempts to control water permeation through membranes, mainly polymeric, concentrate on modulating membrane's structure and physicochemical properties of its surface by varying pH, temperature and ionic strength[3,8]. Electrical control over water transport offers an attractive alternative stimulus; however, theory and simulations[9-14] have often yielded conflicting results from freezing of water molecules to melting of ice[14-16] under applied electric field. Here we report electrically controlled water permeation through micrometre-thick graphene oxide (GO) membranes[17-21] which exhibit ultrafast permeation of water[17,22] and unique molecular sieving properties[18,21] with the potential for industrial-scale production. To achieve electrical control on water permeation, conductive filaments are created in GO membranes by controllable electric breakdown. The electric field concentrated around such current carrying filaments leads to ionisation of water molecules in graphene capillaries, allowing precise control of water permeation: from ultrafast permeation to complete blocking. The unforeseen electrical control on water permeation through GO membranes in this work has profound significance in understanding and controlling the dynamics of water molecules in nanocapillaries without involving complicated chemical modifications and, opens up an avenue for developing smart membrane technologies for artificial biological systems, tissue engineering and filtration.

Our devices are essentially GO membranes with metal electrodes on both sides, fabricated by depositing a thin ($\approx$ 10 nm) gold (Au) film on top of the GO membrane prepared on a porous silver (Ag) substrate (Extended Data Fig. 1). Such a thin layer of gold is sufficiently porous and practically does not change the ultrafast water permeation (slip enhanced flow as seen in ref. 17

and 22) properties of the GO membranes (Extended Data Fig. 1d). For details of device fabrication and permeation experiments, we refer to Methods sections: 'Fabrication of metal-GO-metal membranes' and 'Permeation experiments'. Figures 1a,b show a schematic and an optical photograph of our membrane device.

In order to increase the electric field applied up to the values sufficient for water dissociation, thin conductive filaments were introduced in our membranes by controllable electric breakdown. We attribute this conductive filament formation to the presence of moisture in GO membranes which often known to facilitate the formation of conducting paths (generally carbon) across the insulators under large electric fields[23] (see Methods section 'Conducting filament formation'). Fig. 1b shows the $I\text{-}V$ characteristics of the device exposed to 100% relative humidity (RH) during the filament formation. Up to a critical voltage, V_c, the current does not change appreciably. However, at V_c (~2 V for the sample in Fig. 1 and varied by 25% for four different samples studied) a partial electrical breakdown occurred, evident through a sudden current increase up to the compliance level. This breakdown state is stable and, characterised by low transversal resistance.

After the controllable breakdown, the $I\text{-}V$ characteristics are nearly ohmic and suggest the existence of permanent electrically conductive channels (Fig. 1b). However, the in-plane $I\text{-}V$ measurements did not show any significant change in conductivity compared with pristine samples (Extended Data Fig. 2b). Unlike in-plane conductivity, the out-of-plane conductivity was found to be stable and insensitive to the humidity of the environment (Extended Data Fig. 2b). This confirms the formation of conducting filaments (e.g., carbon filaments) between the electrodes (out-of-plane) that are not connected in the plane of the membrane. Further, our peak force tunnelling atomic force microscopy (PF TUNA) and Raman spectroscopy (See Methods section 'Characterization of conducting filaments') experiments have clearly shown the presence of conductive filaments of diameter < 50 nm (Fig. 1d and Extended Data Figs. 3,4), with filament density ~10^7/cm^2. Note that no significant changes were observed in the chemical stoichiometry of the GO membrane (as measured by X-ray photoelectron spectroscopy (XPS)), except for a small increase in the C/O ratio (3.2 to 3.6) on the membrane surface closest to the positive electrode. The C/O ratio of all other membrane surfaces remains the same as the pristine sample (see Methods section 'XPS' and Extended Data Fig. 5).

To probe the influence of electric field on water permeation through pristine GO membrane, the applied voltage was increased stepwise which allowed monitoring both current and water permeation as a function of time during filament formation process. At each voltage step, measurements were carried out for a minimum period of four hours. Fig. 1e shows the weight loss of the sealed container and the corresponding water permeation rate during the filament formation process. No appreciable change in water permeation rate was found up to V_c (Fig. 1e). At V_c, a sudden decrease (15 times) in water permeation was observed after the partial breakdown of GO membrane. Hereafter, the water permeation through the membranes with the low transverse resistance has shown a strong dependence on the applied voltage, decreasing with increased voltage. At zero voltage, the water permeation mostly recovered (~85%) to the initial value of the pristine sample. The water vapour permeance of GO membrane corresponds to this permeation rate is 6.5 L/h/m^2/bar, ~2 times higher than the commercial polyamide thin film membranes with 10 times smaller thickness (Extended Data Fig. 1d).

The stable out-of-plane electrical conductivity of the membrane and the electrical control of water permeation are more evident from the continuous forward and backward voltage sweeps performed after the filament formation (Fig. 1f). The electrically controlled water permeation is

found to be independent of the polarity of the applied voltage and is completely reversible even after multiple voltage cycles switching between 0 and 1.8 V (Fig. 1f left inset) and a long term switching off (Fig. 1f right inset). The electrical control of water permeation was further confirmed by mass spectrometry (See Methods section 'Mass spectrometry' and Extended Data Fig. 6). It is also noteworthy that the observed electrical control can be extended to the case of liquid water permeation (see Methods section 'Electrical control on liquid water permeation' and Extended Data Fig. 7).

To understand the influence of voltage and current on water permeation, we have performed additional experiments using GO membranes with different permeation area and thickness. Fig. 2a shows water permeation rate as a function of current through GO membranes with 1 μm thickness but with two different permeation areas. Here, the four times smaller membrane requires only a quarter of the current compared with large membrane to achieve same level of water blockage, suggesting current density through the membrane is the crucial factor in controlling water permeation. Fig. 2b shows normalized water permeation rate as a function of current, through 1 μm and 5 μm thick GO membranes with same permeation area. Here, the decrease in normalized water permeation rate was found to be nearly identical for the same magnitude of electric current passing through both the membranes. However, the voltage required to maintain the same magnitude of current is significantly different, indicating direct correlation between water permeation rate and electric current rather than applied voltage. Both these observations confirm the current control on water transport in our experiments rather than applied voltage.

The influence of the current on the water transport can be due to Joule heating, dewetting or possible electrochemical changes. We have measured the membrane temperature as a function of the electric current across the membrane (see Methods section 'Joule heating effect') and found no significant variations (Extended Data Fig. 8a). Further, we have ruled out the prospect of changes in GO wetting properties, as *in-situ* water absorption experiments confirm the absence of significant changes in weight intake at 100% RH even in the presence/absence of electric current (dewetting could cause decrease in weight) (see Methods section '*In-situ* water absorption/release' and Extended Data Fig. 8b). In order to test the electrochemical mechanism, we measured the water infrared (IR) modes from the GO membrane for a varying electric current across it (Fig. 3a and see Methods section '*In-situ* IR measurements'). The pristine sample shows three main characteristic IR bands peaked at ~1620, 1737 and 3500 cm^{-1}, which correspond to the deformation vibration of adsorbed water molecules, the carbonyl (C=O) stretching mode of carboxylic group itself and, the O-H stretching mode in both the GO sheets and the interspersed water molecules, respectevely[24-26]. Interestingly, all the band intensities associated with water molecules decreased when an electric current is switched on and, fully recovered to their initial values (Fig. 3a inset) when the current brought to zero. However, the band intensity relating to carbonyl groups remains constant.

To test if the decrease in the IR water signal is associated with the reduced amount of water, we performed X-ray diffraction (XRD) study in the presence of electric current in our membrane devices[21] (see Methods section '*In-situ* XRD measurements'). Fig. 3b shows the *in-situ* changes of the (001) reflection as a function of the current across the membrane with the (001) peak clearly shifting to higher 2θ values at elevated currents. The interlayer spacing, *d*, is estimated from the XRD analysis, and plotted as a function of electric current in Fig. 3c. We found a decrease in *d* from 9.2 Å to 8.5 Å as the current across the membrane increases from zero to 25 mA. Note that these electric current induced changes in *d* were also found to be reversible (Fig. 3d) and, did not

present during the first voltage sweep up to V_c, before the filament formation. However, the observed small change in d (0.7 Å) is not expected to significantly affect the water permeation in GO membranes due to the slip-enhanced water permeation through graphene capillaries[17,22], and also, cannot explain the observed reduction (nearly 50%) in the IR peak intensity.

Based on these observations, we attribute the electrically controlled water permeation to current-mediated ionisation of water molecules. It is known that a current-carrying conductor produces an electric field around it[27,28] (see Methods section 'Electric field due to a current-carrying conductor'). The exact value of electric field depends on the parameters of the set-up, but for a coaxial arrangement (current flows in one direction through the inner conductor of radius a and, in the other direction through a coaxial conductor of radius b—in our case the characteristic size of the sample), the radial component of the field is given by

$$E_r = \frac{Jz}{\sigma r} \frac{1}{ln(a/b)}$$

where J is the current density, z varies from 0 to L—length of the wire (thickness of the membrane), r is the radial distance from the centre of the wire, and, σ is the electrical conductivity of the wire[27,28] (Extended Data Fig. 9a). In our case this formula reduces to $E_r = (V/r) \cdot (1/ln(a/b))$, and it is obvious that close to the surface of the filaments (r is of the order of few tens nm) the electric field can be as high as $\sim 10^7$ V/m (Extended Data Fig. 9b). Such large electric fields could dissociate water molecules to produce hydronium (H_3O^+) and hydroxyl (OH^-) ions (See Methods section 'Electric-field-induced dissociation of water'), with the effect becoming more pronounced at higher currents.

Further, MD simulations performed for understanding the influence of H_3O^+ and OH^- ions on water permeation show that the water permeation rate in graphene capillary decreases with increasing the ion's concentration (See Methods section 'MD simulations' and Extended Data Fig. 10). This could be attributed to two main effects: (i) the localization of H_3O^+ and OH^- ions inside the capillary, due to their interaction with graphene/GO, which creates local blockage; (ii) the formation of large hydrated clusters due to strong interactions between H_3O^+/OH^- ions and surrounding water molecules, which impedes the water transport. Our first-principles calculations[29] confirmed that the latter is the dominant effect because of strong hydrogen bond between the ions and surrounding water (Fig. 4a-d and see Methods section 'Interaction of H_3O^+/OH^- ions with water and graphene/GO capillary'). In agreement with this modeling results, additional liquid water permeation experiments clearly demonstrated that simultaneous presence of both H_3O^+ and OH^- ions are necessary to achieve reduction in water permeation rate (Fig. 4e,f and see Methods section 'Influence of H_3O^+/OH^- ions'). This is consistent with previously reported cooperativity effect[30], where the simultaneous presence of strongly hydrated cations and anions decreases the mobility of water molecules and changes their dynamics. The proposed model of electric field enhanced dissociation of water is also consistent with the observed reversible chemical changes in the interlayer water molecules (IR peak intensities) and the changes in the interlayer spacing (Fig. 2b) with current. This could be attributed to the changes in the structure of interlayer water due to the ionisation. Further experimental and theoretical efforts are needed for a comprehensive understanding of the exact mechanism responsible for electric current control on water permeation.

References

1   Karnik, R. *et al.* Electrostatic control of ions and molecules in nanofluidic transistors. *Nano Letters* **5**, 943-948 (2005).

2   Gravelle, S. *et al.* Optimizing water permeability through the hourglass shape of aquaporins. *Proc. Natl. Acad. Sci.* **110**, 16367-16372 (2013).

3   Liu, Z., Wang, W., Xie, R., Ju, X.-J. & Chu, L.-Y. Stimuli-responsive smart gating membranes. *Chem. Soc. Rev.* **45**, 460-475 (2016).

4   Xiao, K. *et al.* Electrostatic-charge- and electric-field-induced smart gating for water transportation. *ACS Nano* **10**, 9703-9709 (2016).

5   Wang, Z., Ci, L., Chen, L., Nayak, S., Ajayan, P. M. & Koratkar, N. Polarity-dependent electrochemically controlled transport of water through carbon nanotube membranes. *Nano Lett.* **7**, 697-702 (2007).

6   Hetherington, A. M. & Woodward, F. I. The role of stomata in sensing and driving environmental change. *Nature* **424**, 901-908 (2003).

7   Borgnia, M. J., Nielsen, S., Engel, A. & Agre, P. Cellular and molecular biology of the aquaporin water channels. *Annu. Rev. Biochem.* **68**, 425-458 (1999).

8   Zhao, C., Nie, S., Tang, M. & Sun, S. Polymeric pH-sensitive membranes—A review. *Prog. Polym. Sci.* **36**, 1499-1520 (2011).

9   Kou, J. *et al.* Electromanipulating water flow in nanochannels. *Angew. Chem. Int. Ed.* **54**, 2351-2355 (2015).

10   Li, J. *et al.* Electrostatic gating of a nanometer water channel. *Proc. Natl. Acad. Sci.* **104**, 3687-3692 (2007).

11   Gong, X. *et al.* A charge-driven molecular water pump. *Nat. Nanotechnol.* **2**, 709-712 (2007).

12   Vaitheeswaran, S., Rasaiah, J. C. & Hummer, G. Electric field and temperature effects on water in the narrow nonpolar pores of carbon nanotubes. *J. Chem. Phys.* **121**, 7955-7965 (2004).

13   Saitta, A. M., Saija, F. & Giaquinta, P. V. *Ab* initio molecular dynamics study of dissociation of water under an electric field. *Phys. Rev. Lett.* **108**, 207801 (2012).

14   Qiu, H. & Guo, W. Electromelting of confined monolayer ice. *Phys. Rev. Lett.* **110**, 195701 (2013).

15   Choi, E.-M., Yoon, Y.-H., Lee, S. & Kang, H. Freezing transition of interfacial water at room temperature under electric fields. *Phys. Rev. Lett.* **95**, 085701 (2005).

16   Diallo, S. O., Mamontov, E., Nobuo, W., Inagaki, S. & Fukushima, Y. Enhanced translational diffusion of confined water under electric field. *Phys. Rev. E* **86**, 021506 (2012).

17   Nair, R. R., Wu, H. A., Jayaram, P. N., Grigorieva, I. V. & Geim, A. K. Unimpeded permeation of water through helium-leak–tight graphene-based membranes. *Science* **335**, 442-444 (2012).

18   Joshi, R. K. *et al.* Precise and ultrafast molecular sieving through graphene oxide membranes. *Science* **343**, 752-754 (2014).

19   Sun, P., Wang, K. & Zhu, H. Recent developments in graphene-based membranes: structure, mass-transport mechanism and potential applications. *Adv. Mater.* **28**, 2287-2310 (2016).

20   Liu, G., Jin, W. & Xu, N. Graphene-based membranes. *Chem. Soc. Rev.* **44**, 5016-5030 (2015).

21   Abraham, J. *et al.* Tunable sieving of ions using graphene oxide membranes. *Nat. Nanotechnol.* **12**, 546-550 (2017).

22   Radha, B. *et al.* Molecular transport through capillaries made with atomic-scale precision. *Nature* **538**, 222-225 (2016).

23   Kao, K.-C. *Dielectric phenomena in solids : with emphasis on physical concepts of electronic processes*. (Academic Press, 2004).

24   Acik, M. *et al.* The role of oxygen during thermal reduction of graphene oxide studied by infrared absorption spectroscopy. *J. Phys. Chem. C* **115**, 19761-19781 (2011).

25   Hontoria-Lucas, C., López-Peinado, A. J., López-González, J. d. D., Rojas-Cervantes, M. L. & Martín-Aranda, R. M. Study of oxygen-containing groups in a series of graphite oxides: Physical and chemical characterization. *Carbon* **33**, 1585-1592 (1995).

26   Konkena, B. & Vasudevan, S. Understanding aqueous dispersibility of graphene oxide and reduced graphene oxide through pKa measurements. *J. Phys. Chem. Lett.* **3**, 867-872 (2012).

27   Jackson, J. D. Surface charges on circuit wires and resistors play three roles. *Am. J. Phys.* **64**, 855-870 (1996).

28   Marcus, A. The electric field associated with a steady current in long cylindrical conductor. *Am. J. Phys.* **9**, 225-226 (1941).

29   Liang, C. et al. Ion sieving in graphene oxide membranes via cationic control of interlayer spacing. *Nature* **550**, 380-383 (2017).

30   Tielrooij, K. J., Garcia-Araez, N., Bonn, M. & Bakker, H. J. Cooperativity in ion hydration. *Science* **328**, 1006–1009 (2010).

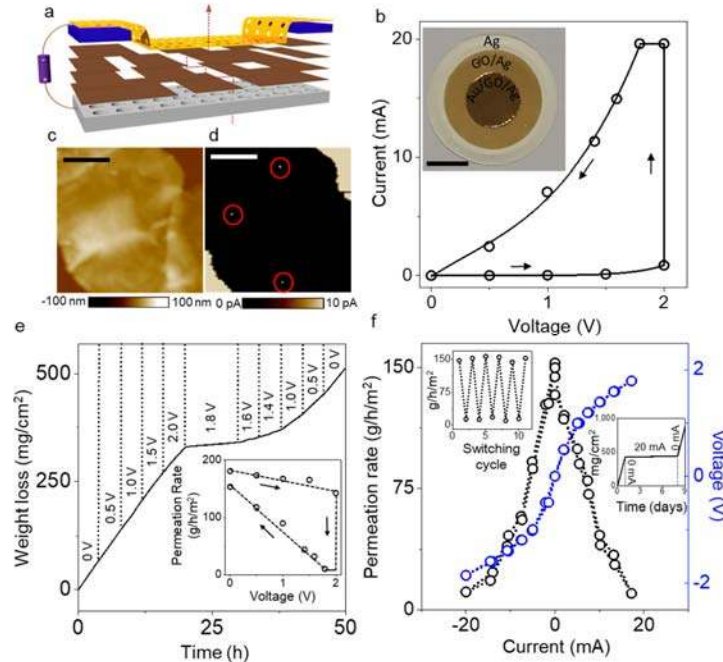**Figure 1| Electrically controlled water permeation through a GO membrane. a**, Schematic showing a GO membrane (deposited on porous Ag substrate) with voltage applied. The yellow, blue and brown layers represent the porous Au electrode, a plastic mask (avoids electric shorting between Au and Ag electrodes) and GO sheets, respectively. The dotted line shows a possible pathway for water permeation. **b**, *I-V* characteristics at 100% RH during the first voltage sweep showing a sudden increase in current, suggesting partial electrical breakdown of the GO membrane and conducting filament formation. The solid line is a guide to the eye and arrows indicate the direction of the voltage sweep. Inset: Photograph of a GO membrane showing the central sandwiched (Au/GO/Ag) region, the GO on supporting Ag, and the bare Ag substrate. The plastic mask outside the Au layer is removed for clarity. The outer area of the central sandwiched region was masked to block water permeation through this region (Extended Data Fig. 1a,b). Scale bar: 5 mm. **c**, Topography and **d,** the corresponding PF TUNA current image of a conducting GO membrane exfoliated on a Au thin film coated Si substrate. The conducting filaments (size ranging from 20 to 45 nm) formed in the GO membrane are marked by red circles. Scale bars: 1 μm. **e**, Weight loss for a water-filled container sealed with a 1 μm thick GO membrane (7 mm diameter) at different voltages applied across the membrane during the filament formation process. Inset: Water permeation rate through the GO membrane as a function of applied voltage. Arrows indicate the direction of voltage sweep. **f**, Water permeation rate as a function of the current across the GO membrane after the filament formation, and the corresponding *I-V* characteristics (color-coded axis). One complete voltage sweep for both positive and negative polarity is plotted. Left inset, continuous switching between 0 and 1.8 V showing the stability of permeation control. Right inset, weight loss data showing the stability of long-term switching off (7 days) and the subsequent recovery. All weight loss measurements were performed inside a dry chamber with 10% RH.
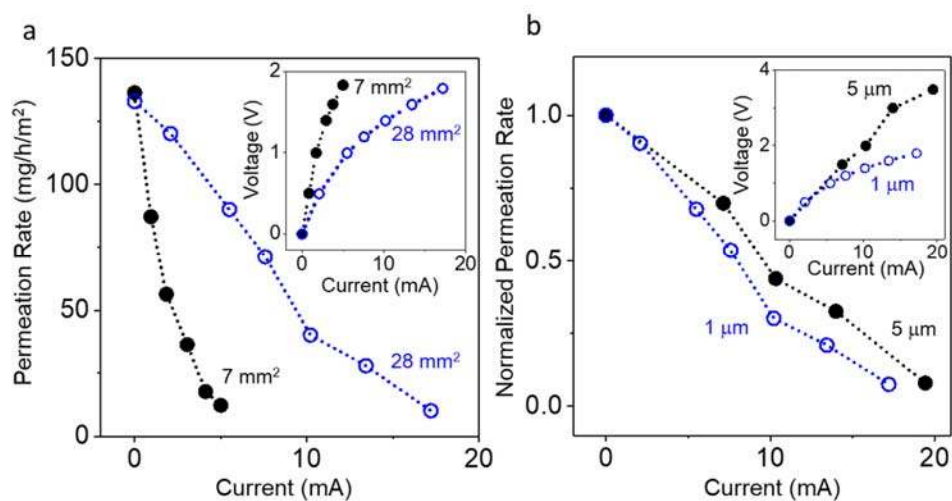
Figure 2| Current controlled permeation. a, Permeation rate as a function of the current through two GO membranes with different areas (28 mm^2 and 7 mm^2). **b,** Normalized water permeation rate as a function of the current through GO membranes with two different thicknesses. Permeation rates were normalized with respect to zero applied voltage because the absolute water permeation rates of 1 μm and 5 μm GO membranes were different. Insets in **a** and **b** show the corresponding *I-V* characteristics.
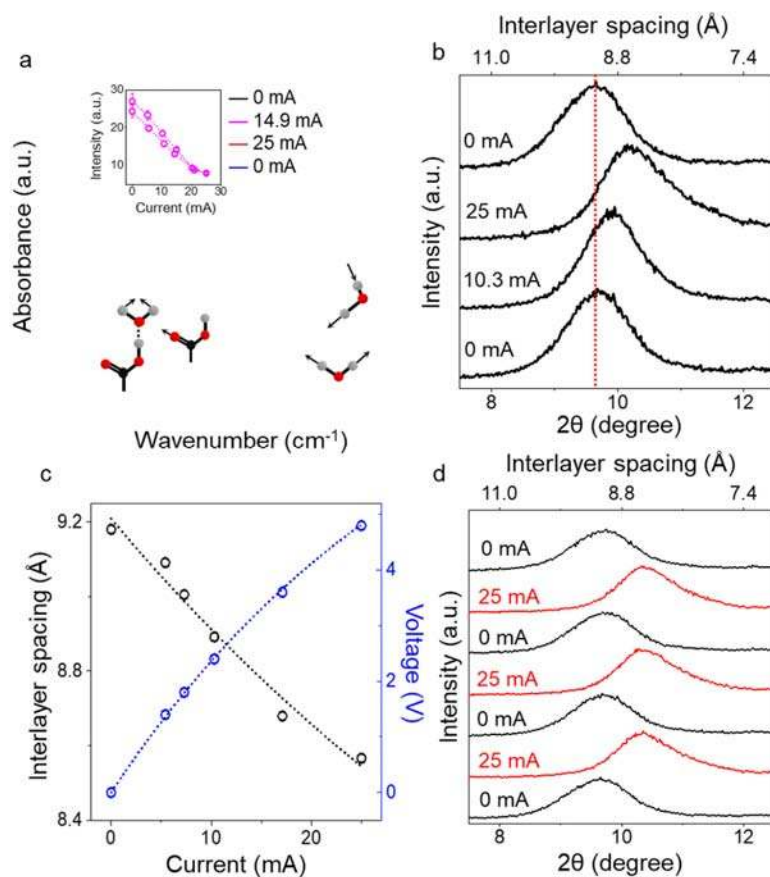
Figure 3| *In-situ* FTIR and X-ray measurements. a, *In-situ* FTIR spectrum acquired from a GO membrane in which the current was cycled as 0 mA→14.9 mA→25 mA→0 mA. Inset: Peak intensity (area under the curve) as a function of the current for the peak at ~3500 cm^{-1} in forward and backward sweeps. The ball-and-stick models below the data illustrate the vibrational modes responsible for the different IR peaks. Red–Oxygen, Black–Carbon, and Grey–Hydrogen. **b**, X-ray diffraction for different current levels across the 10 μm thick GO membrane (membrane diameter ~10 mm). **c**, Changes in the interlayer spacing as a function of current and the corresponding *I-V* behavior of the membrane (color-coded axis). The dotted lines are guide to the eye. **d**, Reversible switching of the (001) X-ray peak with the current.
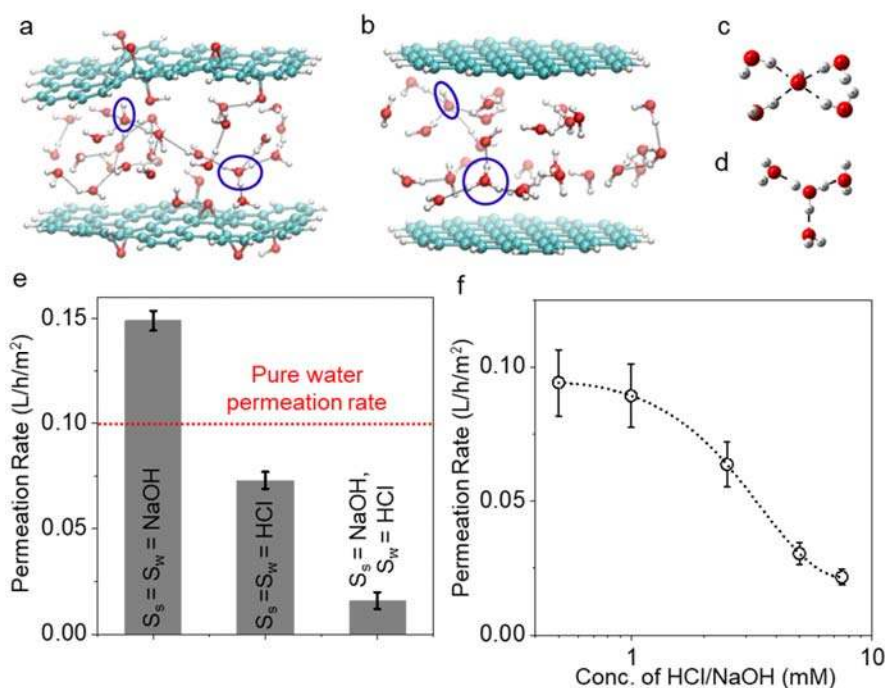
Figure 4| Influence of H_3O^+ and OH^- ions on water dynamics inside nanochannels: The first-principles optimized configuration for confined water in the presence of H_3O^+ and OH^- ions inside **a,** GO and **b**, graphene nanochannel with a height of 1 nm. White, cyan and red color spheres represent hydrogen, carbon and oxygen atoms, respectively. The black color dashed lines represent hydrogen bonds. Circles show H_3O^+ and OH^- ions. **c,** First hydration shell of OH^- and **d**, H_3O^+ ions inside nanochannel. **e,** Osmotic pressure driven liquid water permeation rate in the presence of NaOH and/or HCl in water and sucrose compartments separated by a GO membrane. NaOH/HCl solutions added to water, and sucrose compartments are denoted as S_w and S_s, respectively. Red dotted line indicates water permeation rate when NaOH and HCl are absent. **f,** Water permeation rate as a function of concentration of both NaOH and HCl in the sucrose and water compartment, respectively. Error bars, standard deviations from three different measurements using different membranes. The dotted line is a guide to the eye.

Author contributions: R.R.N. initiated and supervised the project. K.-G.Z. performed the experiment and analyzed the data with help from K.S.V. and R.R.N; K.S.V. carried out PF TUNA and Raman characterisation and analysis. C.T.C. carried out mass spectroscopy. K.H., J.A. and Y.S. helped in sample preparation, characterization and data analysis. K.S.V., M.N., H.G., K.S.N. and F.M.P. performed theoretical modelling and simulations. J.C.Z. and A.P. performed the XPS characterizations. O.P.M., V.G.K. and A.N.G. performed infrared characterizations. A.K.G.

contributed to theoretical discussions. R.R.N., K.S.V., K.-G.Z. and K.S.N. co-wrote the paper. All authors contributed to discussions.

Methods

Fabrication of metal-GO-metal membranes. GO aqueous dispersions (flake size of ≈ 10 µm) were prepared by exfoliation of graphite oxide powder (BGT Materials Limited) in water using bath sonication[17,21]. Different steps in the fabrication process and an optical photograph of the metal-GO-metal sandwich membrane are shown in Extended Data Fig. 1a,b. First, a Sterlitech porous silver metal membrane (0.2 µm pore size and 13 mm diameter), which also acts as the bottom electrode, was used in a standard vacuum filtration set-up to prepare GO membranes for the permeation experiments. These membranes were glued (using Stycast 1266 epoxy resin) onto the polyethylene terephthalate (PET) films (step 1 in Extended Data Fig. 1a) with a circular aperture (diameter of ~1 cm) before depositing a thin (~10 nm) top Au electrode (step 2 in Extended Data Fig. 1a) using thermal evaporation at a deposition rate of 0.8 Å/s in a high vacuum chamber (2×10^{-6} mbar) at temperature 20 ± 1°C. Here, the PET film prevents electrical shorting between the top and bottom electrodes in the metal-GO-metal sandwich membrane structures. Finally, these structures were glued onto another plastic disc (step 3 in Extended Data Fig. 1a) which provides mechanical support for sealing the sample to a stainless steel water container used in pervaporation experiments[17].

Permeation experiments. We employed a previously reported gravimetric method[17] to probe the electrical effects on water permeation through GO membranes. A plastic disc containing the metal-GO-metal sandwich membrane was fixed to a stainless steel water container using two rubber O-rings to ensure an air-tight seal. The water permeation rate was measured in terms of weight loss of the water container using a computer-controlled precision balance (Mettler Toledo; accuracy 0.1 mg). All the gravimetric experiments were carried out in a chamber with a controlled RH of 10%.

To probe electrical effects on water permeation, thin copper wires extending from both the electrodes were connected to a Keithley 2410 sourcemeter (Extended Data Fig. 1a). An additional Keithley 2182A Nanovoltmeter was also connected across the membrane to measure the potential drop. During permeation experiments a current compliance (20 mA for the sample in Fig. 1) was set to limit the current density to a maximum of 70 mA/cm^2 for preventing uncontrollable breakdown (blustering) of the device.

To study the influence of Au electrode on the water permeation rate, we deposited thin Au layers (10 to 50 nm) on 1 µm thick GO membranes. Extended Data Fig. 1c shows the scanning electron microscope (SEM) image of 10 nm Au film on GO membrane, which clearly displays different types of uniformly distributed pores (discontinuities and voids) occupying $\approx 40\%$ of the total area of Au film. Despite uniform pore distribution, 10 nm Au thin films still show conductivity of 3.7×10^6 Ω^{-1} m^{-1} (~ 9% of bulk conductivity)[31], enabling their use as electrodes. These Au electrodes become continuous with decreased porosity (Extended Data Fig. 1d inset) as their thickness increases.

As expected, the permeation rate of 1 μm thick GO membrane on porous Ag support (before Au electrode deposition) is found to be approximately same as that of bare porous Ag support[17] (Extended Data Fig. 1d). The water permeation rate decreased only by a factor of ≈1.5 after depositing Au electrode of thickness ≈10 nm on the GO membrane. However, with increasing thickness of Au electrode, the water permeation rate of Au/GO/Ag membranes decreases exponentially (Extended Data Fig. 1d) due to decreased pore size of the electrode. It is also noteworthy that the water permeation rate of Au/GO/Ag membranes with 10 nm Au electrode is ≈2 times greater than that of commercial polyamide nanofiltration membrane (NF Polyamide-TFC, 200-400 Da, Dow Filmtec™) (Extended Data Fig. 1d).

Conducting filament formation. Controllable dielectric breakdown of the GO membrane was performed by setting appropriate current compliance during the first voltage sweep across the membrane. Extended Data Fig. 2a shows I-V characteristics of the GO membranes at different RH in the first voltage sweep. Similar to tracking phenomenon in dielectrics[23,32,33], we found that conducting filament formation in GO membranes is also highly sensitive to humidity of the environment. The sample exposed to zero humidity did not show any evidence of the formation of electrically conducting filaments even up to 50 V, confirming high dielectric strength of GO in a dry atmosphere[34,35]. However, the samples exposed to humid conditions deviate from this behavior, showing a sudden increase in the current at V_c, where the samples were permanently switched to a conducting state with stable out-of-plane conductivity even in the negative bias conditions (Fig. 1f). The decrease in value of V_c with increasing humidity of the environment (Extended Data Fig. 2a) further suggests the contribution of absorbed water content (interlayer water) in formation of the conducting filaments inside GO membranes.

It is noteworthy that similar conducting filament formation was previously observed in dried GO thin films (thickness varied from 10 to 100 nm) used for the fabrication of resistive random-access memory (ReRAM) devices. Nearly two orders of magnitude higher electric field across such thin films, compared with the field across our micrometer-thick GO membranes, causes the filament formation in dry conditions. Importantly, the filament formation in ReRAM devices is completely reversible due to the current induced heating effects[36,37], and GO thin film turns into electrically insulating once polarity of the applied voltage changes. However, the filament formation in GO membranes in this study is permanent and the membranes remain permanently conducting regardless of the changes in polarity of applied voltage (Fig. 1f). Micron length filaments and high filament density (~10^7/cm^2) in our GO membranes limit the current flow (see below) through each filament to a small value (~1 nA), and hence the membranes stays in permanently conducting state due to negligible current induced heating effects.

For further understanding of electrical conductivity in GO membranes after the filament formation, we have measured the in-plane conductivity of GO membrane that displayed out-of-plane conductivity. For this, the membrane was peeled off from the silver substrate and then exfoliated using scotch tape. A pair of electrodes (3 mm apart with a width of 1 cm) was made on this freshly peeled GO membrane using conductive silver paste to measure the in-plane conductivity. Extended Data Fig. 2b compares the out-of-plane and in-plane I-V characteristics of the GO membrane after conducting filament formation. Surprisingly, we found that the in-plane electrical conductivity of these GO membranes is similar to that of highly resistive pristine GO membranes (~15 μS/cm)[38]. In addition, after filament formation, the stable out-of-plane I-V characteristics of GO membrane (inset of Extended Data Fig. 2b) recorded at 0% RH and 100% RH have shown humidity independent out-of-plane electrical conductivity, unlike the in-plane electrical conductivity in

11

GO[39]. This clearly confirms the permanent filament formation. Additional experiments carried out after exposing the GO membrane containing filaments to 30 bar external pressure using nitrogen gas in the high-pressure vessel, didn't show any change in out-of-plane electrical conductivity and the electrical control on water permeation—establishing the stability of permanent conducting filaments.

Characterization of conducting filaments. To demonstrate the existence of conducting filaments inside the GO membranes, the top and bottom metal electrodes were peeled off using a scotch tape. These GO membranes were further exfoliated using scotch tape to obtain the freshly cleaved inner surface for characterization using SEM, XPS, energy dispersive X-ray (EDX) and Raman spectroscopy. The SEM image of a conducting GO membrane shown in Extended Data Fig. 3a exhibits the texture similar to pristine GO membrane with no noticeable features corresponding to the conducting filaments. EDX analysis also confirms the presence of only carbon and oxygen elements in the membrane.

Raman spectra of the GO samples were collected using HORIBA's XploRA PLUS Raman spectrometer with 1800 lines/mm grating and 532 nm laser excitation at a power of 1.35 mW. Extended Data Figs. 3b,c show the Raman I_D/I_G mapping for a pristine GO membrane and a GO membrane (close to the positive electrode) with conducting filaments (conducting GO membrane). I_D/I_G represents the ratio of intensities correspond to D band at 1351 cm^{-1} and G band at 1594 cm^{-1} in the Raman spectrum (Extended Data Figs. 3e,f). As shown in Extended Data Fig. 3b, I_D/I_G value is uniform (0.93) over the whole area of 10 μm × 10 μm in the case of pristine GO sample. However, for the GO membrane with conducting filaments, I_D/I_G was found to be inhomogeneous (Extended Data Fig. 3c) and varied from 0.93 (blue-colored areas) to 1.1 (green-colored areas) at different positions on the sample. A similar increase in I_D/I_G was reported for the reduction of GO and, attributed to an increase in the *sp²* carbon network[40]. This suggests that the conducting filaments across the GO membrane are made of *sp²* carbon.

To investigate the uniformity of carbon filaments across the top and bottom electrodes, we have carried out I_D/I_G mapping experiments on a conducting GO membrane surface close to the negative electrode, obtained by multiple peelings of the membrane. The I_D/I_G map acquired from the surface close to negative electrode (Extended Data Fig. 3d) shows significant reduction in the size of domains correspond to high I_D/I_G ratio (~1.1), suggesting the shrinkage of carbon filaments towards the negative electrode. This is further corroborated from the estimated *sp²* carbon content in XPS analysis (see Methods section 'XPS'). In addition, it is apparent from Extended Data Fig. 3c,d that several filaments are formed in each GO flake (of size ~10 μm × 10 μm). The number of conducting filaments estimated by counting bright spots in Extended Data Fig. 3d is ~10^7/cm^2.

Further, we have carried out atomic force microscopy (AFM) imaging using Bruker Dimension ICON AFM operated in PF TUNA mode (with Pt/Ir coated Bruker's PF TUNA probes) to confirm filament formation in conducting GO membranes. Pristine GO membrane was used as a reference. Particularly, the surface close to the negative electrode of conducting GO membranes was exfoliated onto Cr/Au (5 nm/95 nm) thin film deposited Si substrate to perform PFTUNA experiments. This facilitates the application of a constant DC bias (3 to 5 V with variable gain setting of 10^9 to 10^{10} V/A) between the sample and AFM probe. The current passing through the sample between Cr/Au thin film and the AFM probe is measured using a current sensor, when the probe and sample are intermittently brought into contact. Thus, the mapping of electrical current across the samples provides TUNA current image along with topography.

Extended Data Figs. 3g,i show height images of the pristine and conducting GO (prepared at 100% RH) membranes exfoliated on the Cr/Au deposited Si substrate. Their corresponding TUNA current images are shown in Extended Data Figs. 3h,j. Topography of both the membranes in height images did not show any significant difference and the measured thickness of membranes was varied between ~30 to 40 nm. However, the TUNA current images of pristine and conducting GO membranes exhibited considerable differences. In the case of pristine GO membrane, an apparent contrast was observed for GO (dark regions) from the surrounding gold thin film (bright region) as the magnitude of TUNA current between gold thin film and the probe is much higher than that between GO and the probe. On the other hand, TUNA current images (Fig. 1 and Extended Data Fig. 3j) obtained from conducting GO membranes (ten different areas of three samples) clearly display the presence of small conducting regions (which cannot be identified in height images) within non-conducting GO (dark) region. Further, the filament density $~10^7/cm^2$ estimated by counting such conducting regions in TUNA current image is in good agreement with Raman analysis.

Based on Raman and PF TUNA experiments, we propose the structure of conducting filaments as the parallel resistor model (Extended Data Fig. 3k). To validate this model, we have divided a large conducting GO membrane (7 mm diameter) into four equal pieces. We found that the resistance of four individual pieces is relatively same in magnitude and, four times greater than that of large parent membrane (Extended Data Fig. 3k) but with similar resistivity. This clearly confirms the uniform distribution of conducting filaments inside GO membrane, supporting the parallel resistor model.

Additional PF TUNA images (Extended Data Figs. 4b,d) obtained from the GO membranes with filament formation occurred at 40%RH and inside liquid water (Extended Data Fig. 7), clearly confirm the influence of intercalated water on conducting filament number density. Increased water content of GO membranes found to increase the filament density and also the diameter.

For further understanding on filament formation, we have carried out additional experiments on partially reduced GO (prGO) membranes (Extended Data Fig. 4e), prepared by annealing GO membranes (prior to top electrode deposition) at 90 °C in an inert atmosphere. GO membrane annealed at 90°C, showed one order increase in out-of-plane electrical conductivity, however, did not show any metallic behavior—indicating only a partial reduction in oxygen content; whereas, GO membrane annealed at 120°C became ohmic and, did not exhibit filament formation.

I-V characteristics (Extended Data Fig. 4e) of Au/prGO/Ag membrane during first voltage sweep at 100% RH has shown significantly small V_c (less than 1 V) compared with pristine GO membranes. Interestingly, PF TUNA current image of prGO membrane after the filament formation (Extended Data Fig. 4f) has shown conducting filaments of ~3 times larger diameter, but, with a conducting filament density ($2.4\times10^7/cm^2$), approximately equal to that of pristine GO membranes. Decreased V_c and the formation of wider filaments in prGO membranes could be attributed to the increased conducting graphitic regions after partial reduction, consistent with the previously reported conducting islands activated filament formation mechanism[36,37].

XPS. To investigate the chemical stoichiometry of GO membranes before and after the application of an electric potential (after electrically controlled water permeation experiments), we performed XPS experiments in an ultrahigh vacuum system with a base pressure of $<3\times10^{-10}$ mbar using a monochromated Al Kα source at 1486.6 eV (Omicron XM 1000) and a power of 220 W.

Extended Data Fig. 5a shows XPS spectra from the pristine GO membrane and Extended Data Figs. 5b,c represent XPS spectra of a GO membrane after electrically controlled permeation, acquired from an inner surface of the membrane and a surface close to the positive electrode, respectively. The membrane surface close to the electrode was obtained by removing the Ag electrode through mechanical peeling, and then cleaving the membrane using scotch tape to reveal an inner surface. Using XPS Peak 4.1, each C 1s spectrum was fitted with four components representing the main bonding environments found in GO: C-C (284.5-284.8 eV), C-OH (285.2-285.4 eV), C-O-C (286.3-286.9 eV), and C=O and C(=O)-(OH) (287.8-289.1 eV)[41,42]. We followed the widely accepted peak position assignment and the depiction of XPS peak fitting of GO[41,42], though the different reports follow different representations. C/O ratios calculated from the fitted peak areas were found to be similar (3.2) for pristine GO and the inner surface of the membrane after electrically controlled permeation. In contrast, the membrane surface close to the positive electrode shows an increase in C/O ratio (3.6) indicating a higher sp^2 fraction close to the electrode. C-C fractions are found to be 56% and 63% respectively for the inner surface and from the surface close to the electrode. This increase in sp^2 fraction close to the positive electrode is attributed to the formation of conducting carbon filaments after the application of a voltage across the GO membrane where the concentration of filaments is expected to be large.

Mass spectrometry. Electrical control of water permeation through GO membranes was also confirmed using mass spectrometry (MS). Here, a Au/GO/Ag sandwich structure was placed between two rubber O-rings in a custom made permeation cell (Extended Data Fig. 6a). Copper leads from the top and bottom electrodes were connected to a sourcemeter via an electrical feedthrough. Water vapour (25 mbar) and helium (25 mbar) were fed into the top chamber and permeation through the sample was monitored using MS on permeate side, maintaining at 10^{-6} bar. We used a quadrupole residual gas analyzer (HPR 30 Hiden Analytical) to measure the partial pressure of permeated species and wet cotton in the top chamber as a constant feed for water vapour. Extended Data Fig. 6b shows the partial pressure of water (P_{H2O}), hydrogen, oxygen, and helium (He) in the permeate side at different current through the membrane. No appreciable change in helium partial pressure is observed during voltage cycling, confirming the membrane stability (no damage) under electric field and the impermeability of helium through conducting GO membranes[17]. Extended Data Figs. 6b,c show that P_{H2O} decreases with increasing current through the membrane suggesting a decrease of water permeation through the GO membrane with increasing current which is consistent with the gravimetric measurements. Additionally, the lack of any significant change in H_2 or O_2 partial pressure at the permeate side further indicates that H_2 and O_2 are not released during voltage cycling, ruling out the possibility of electrolysis of water. Extended Data Fig. 6b also confirms the reversible control of water permeation by electrical means.

Electrical control on liquid water permeation. We have carried out osmotic pressure driven water permeation experiments to investigate the electrical control on liquid water permeation through Au/GO/Ag membranes. To this end, Au/GO/Ag membrane was firmly fixed (Extended Data Fig. 7a) between two compartments (one is filled with 12 ml of DI water and other with 1 M sucrose solution) using Stycast 1266 epoxy resin. The liquid water permeation rate (flux) of Au/GO/Ag membrane, calculated from the changes in volume of both the compartments (due to osmotic pressure) as a function of time, is found to be ≈ 0.08 Lh^{-1}m^{-2}, consistent with previous reports[18]. To introduce the conducting filaments in GO membrane, controllable electrical breakdown of Au/GO/Ag membrane was carried out while it is in contact with liquid water.

14

From the *I-V* characteristics shown in Extended Data Fig. 7b, we noticed that V_c for partial electrical breakdown is reduced to 0.8 V for Au/GO/Ag membrane in contact with liquid water, significantly small compared with V_c for the sample at 100% RH. Extended Data Fig. 7c shows the water permeation rate as a function of current and the corresponding *I-V* characteristics. Similar to water vapor permeation rate, liquid water permeation rate is also decreased with increasing electric current, however, only by a factor of 2 even for electric current flow of 40 mA across the membrane. This smaller reduction in liquid water permeation rate compared with water vapor could be understand from the presence of ~25 bar osmotic pressure which makes water to flow faster even in the presence of H_3O^+/OH^- ions and, high number density of filaments (Extended Data Fig. 4d) which limits current flow through each filament to a smaller value, reducing the electric field strength required for dissociation of water.

It is also noteworthy that we were limited to perform electrically controlled liquid water permeation experiments with applied voltages below 1 V. Since the membrane is in contact with liquid water, electrolysis of water takes place once the applied voltage is greater than 1 V and, the released H_2 and O_2 gases at the electrodes damage the membrane.

Joule heating effect. To probe electric-current-induced joule heating, we used an infrared thermometer (N92FX, Maplin Inc.) to monitor the variation of membrane temperature as a function of electric current across the membrane. No significant changes were found in the membrane temperature for each current (Extended Data Fig. 8a). A temperature increase of only ≈ 1 °C was measured for a current of 20 mA which eliminates Joule heating effects in our water permeation experiments.

***In-situ* water absorption/release.** We have performed *in-situ* water absorption experiments on Au/GO/Ag membranes after the filament formation, to understand the changes in GO's wetting properties while electric current flow is set across the membrane. After filament formation, the weight of Au/GO/Ag membrane is continuously measured using a computer controlled balance placed inside an environmental chamber at 35% and 100% RH in the absence and presence of electric current flow. The weight of a completely dried Au/GO/Ag membrane at 0% RH was used as a reference to calculate the weight intake of the membrane at different humidity and electric current.

The weight intake is increased from ≈ 20 to 48% (Extended Data Fig. 8b) as the RH increases from 35% to 100% in the absence of current flow (0 mA) across Au/GO/Ag membrane. We then set an electric current flow of 20 mA across the membrane and, found no significant change in weight intake (Extended Data Fig. 8b) within the experimental accuracy. This clearly suggests the absence of additional water absorption or release of water molecules from the membrane, confirming the absence of changes in GO's wetting properties due to electric current across the membrane (dewetting could have cause a decrease in the weight).

We then decreased the humidity of the chamber to 35% RH while electric current of 20 mA set across the membrane. *In-situ* weight measurements in this state have shown only a small decrease in weight intake (Extended Data Fig. 8b), indicating retention of the majority of absorbed water molecules inside GO membrane. This small decrease in weight intake could be attributed to the evaporation of surface adsorbed water molecules. However, switching the electric current to zero has led to continuous release of the retained water molecules from the GO membrane and reaches to the initial water intake of GO membrane at 35% RH. The retention of water molecules inside the GO membrane in the presence of electric current clearly suggests that the current through the

membrane limits the diffusion of water molecules inside the GO capillaries rather than changing its wetting properties.

***In-situ* IR measurements.** To monitor the chemical changes in GO membranes during voltage cycling, we have performed *in-situ* IR absorption spectroscopy measurements[24] in transmission geometry (typically 512 scans per loop) by employing VERTEX 80, Bruker FT-IR spectrometer and HYPERION Microscope, using a MCT (mercury cadmium telluride) liquid N_2 cooled detector with a mirror optical velocity of 0.6329 cm/s at a resolution of 4 cm^{-1}. To enable the application of electric potential across the membrane during IR measurements, we deposited 10 nm Au electrodes on both sides of the freestanding GO membrane. During IR measurements, the whole system was continuously purged with a dry N_2 stream to remove water in the atmosphere. To match the IR experimental conditions to those of the permeation experiments, we used a water reservoir (a drop of water) at the edge of the GO membranes (away from the IR spot) to hydrate the membrane during measurements. Without this reservoir, IR spectra from the samples resemble that of a dry GO membrane (lower OH vibration peak).

***In-situ* XRD measurements.** For probing the changes in interlayer distance of GO membranes as a function of applied voltage, we have performed *in-situ* XRD experiments using Bruker D-8 Discover advanced XRD system (Cu Kα, λ = 0.154 nm). A homemade XRD sample holder was designed to hold a few milliliters of water beneath the GO membrane, providing a continuous source of moisture to keep the membrane at 100% RH, mimicking experimental conditions similar to electrically controlled water permeation. The interlayer spacing, *d*, was calculated using Bragg's equation, *d=λ/2sinθ*, where θ is scattering angle and λ is wavelength of the incident wave.

Electric field due to a current-carrying conductor. To explain electrically controlled water permeation through GO membranes, we propose a simple model. We consider the case of a single conductive filament of length *L* and radius *a* (*a << L*) carrying a constant stationary current of *I* in a closed circuit with an applied potential of *V*. Current-carrying conductor is known to produce an electric field *E(r,z)* associated with the electric potential *ψ(r,z)* around it, depending on its dimensions and conductivity (*σ*)[27,28,43]. One can envisage that this potential *ψ(r,z)* subsequently decays to zero at a point (at distance *b*) far from the filament. For any point at a distance *r* between *a* and *b*, Laplace's equation is valid[44]:

$$\nabla^2 \psi(r,z) = 0 \qquad\qquad\qquad (1)$$

The boundary conditions for above scenario are $\psi(r,z) = -Jz/\sigma$ and $\partial\psi/\partial z = -E_0 = -J/\sigma$ when $r \leq a$ and $\psi(r,z) = 0$ when $r = b$. Here, *J* is current density through the filament, σ is conductivity of the wire, and *z* varies from 0 to *L* (Extended Data Fig. 9a).

Solving Eq. (1) using the above boundary conditions[28] in cylindrical coordinates (r,ɸ,z) we obtain,

$$\psi(r,z) \;=\; \frac{Jz}{\sigma}\frac{ln(r/b)}{ln(b/a)} \qquad\qquad\qquad (2)$$

The electric field associated with *ψ(r,z)* is calculated as

$$E(r,z) = -\left(\frac{\partial \psi}{\partial r}\hat{r} + \frac{\partial \psi}{\partial z}\hat{z}\right) = \frac{Jz}{\sigma r}\frac{1}{\ln(a/b)}\hat{r} + \frac{J}{\sigma}\frac{\ln(r/b)}{\ln(a/b)}\hat{z} \qquad (3)$$

At very close distances from the filament, the magnitude of the radial component of electric field is higher than that of the z-component. In our experiments, ~1 nA flows through a single conductive filament of $L \approx 1$ µm for an applied potential of 1 V. All these filaments are surrounded by the dielectric GO regions as confirmed from the Raman mapping and AFM experiments. Hence, the electric potential $\psi(r,z)$ decays to zero at some arbitrary radial distance b from the filament. Considering $b = 500$ nm (since the average separation between conductive filaments is ~1 µm, as determined by the Raman measurements) and assuming $a \sim 10$ nm (from PF TUNA imaging), the magnitude of the electric field and its spatial distribution is plotted as a function of r and z in Extended Data Fig. 9b. We found that the field remains high close to the filament (<10 nm) and it decays slightly (by ~6 times) from the top positive electrode (2.3×10^7 V/m) to a point at distance of 100 nm above the bottom electrode (4×10^6 V/m). It is noteworthy that the field around the filament persists even up to a radius of 50 nm with a magnitude varying from 4.3×10^6 V/m to 5.4×10^5 V/m depending on the distance from the top positive electrode. We have also found that for the same 1 nA current, the purely radial component of E decreases by ~40 times as the radius of the filament is increased from 10 nm to 100 nm. In summary, the current carrying filaments in GO membranes produce a radial electric field that is sufficiently strong to dissociate water molecules into OH^- and H_3O^+ ions. Importantly, all of the above estimations are based on a simple model of single straight conducting wire (zero order approximation). However, the complicated structure of conducting filaments could produce even higher electric fields due to the close arrangement of individual filaments, especially near the positive electrode.

Electric-field-induced dissociation of water. Electric field associated dissociation of water[13,45-47] (without producing O_2 and H_2 gas) into H_3O^+ and OH^- ions has previously been observed, even in the presence of transitory fields generated by molecular fluctuations[45]. Based on this, we propose that the strong electric field near the conducting filaments in GO membrane dissociates water in the interlayer channels into OH^- and H_3O^+ ions according to eq. (4).

$$(n + m + 2)H_2O \leftrightarrows OH^- \cdot n(H_2O) + H_3O^+ \cdot m(H_2O) \qquad (4)$$
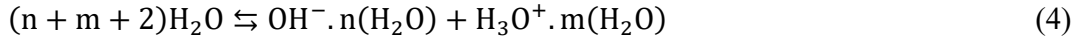
By increasing the electric current in conducting filaments, the electric field (eq. 3) increases and hence the water dissociation rate increases. Once the electric current is switched off, the field vanishes and the reaction kinetics towards left side in eq. 4 becomes more favorable.

The rate of reaction for the ionization in eq. 4 depends on the activation energy. This energy value is known to decrease in the presence of an electric field[47] due to the induced local dipoles in the system, and the water dissociation rate in the presence of electric field is given by

$$k_D(E) = A \exp\left(\frac{-Q(E)}{k_B T}\right) \qquad (5)$$

where A is pre-exponential factor, $Q(E)$ is field dependent activation energy for dissociation, k_B is Boltzmann constant and T is temperature. In a simple form, $Q(E)$ can be expressed as $Q(0)-\Delta Q$, where $Q(0)$ is field-free activation energy for dissociation and ΔQ is field induced decrease in activation energy. Thus, k_D increases with increasing electric field. It is shown from the permeation experiments that water permeation rate P, decreases as the current induced electric field around the conducting filaments is increased. Therefore, $P \propto 1/k_D$ and hence $P(0)/P(E) = exp(\Delta Q/k_B T)$. From the observed change in P due to the electrical current flow (e.g., 20 mA) in our experiments,

we estimated the decrease in activation energy for dissociation of water molecules and it is found to be nearly 12% with respect to the activation energy at room temperature in the absence of an electric field.

MD Simulations. To understand the influence of dissociation of water on the water flow through the GO membranes, we performed non-equilibrium MD simulations. Water permeation through GO membranes is believed to occur along a network of pristine graphene channels that develop between functionalized areas of GO sheets[17] (typically, an area of 40–60% remains free from functionalization[48,49]). Thus, we performed MD simulations using large scale atomic/molecular massively parallel simulator LAMMPS[50], to investigate the dynamical properties (i.e. flow rate) of a mixture of H_3O^+, OH^- and, water inside pristine graphene capillary[17] (Extended Data Fig. 10a).

For MD simulations, the rigid model was used for H_3O^+ and OH^- ions as presented in previous studies[51,52]. The graphene layers were kept fixed and, SPC/E model was employed to describe the water molecules. The carbon and oxygen atoms interact via Lennard-Jones (LJ) pair potentials (σ_C = 0.0553 kcal mol^{-1}, ε_C = 3.4 Å, σ_{H3O+} = 0.147467 kcal mol^{-1}, ε_{H3O+} = 3.05 Å, σ_{OH-} = 0.149618 kcal mol^{-1}, and ε_{OH-} = 3.84 Å) and cross LJ potential parameters were obtained by the Lorentz-Berthelot combining rules. The cut-off radius for LJ potential was chosen at 10 Å. The NVT ensemble (Nosé-Hoover thermostat) was used to control the temperature for both non-rigid and rigid molecules at room temperature. A particle-particle particle-mesh (pppm) was used to compute long-range Coulomb interaction with a desired relative error in the forces for long-range Coulomb interactions solvers of 10^{-4}. In all cases, the time step was chosen as 1 fs. Validation of force fields was confirmed from the calculation of diffusion coefficient of bulk water, D_0 = 2.45×10^{-5} cm^2/s, which is in good agreement with previous experimental results[53].

Extended Data Fig. 10a shows the simulation box, which contains two compartments that are connected by a graphene capillary of height 10 Å. Periodic boundary conditions were applied along z-direction in the boxes and along y-direction in the capillary. The simulation unit cell contained 4362 water/ion molecules and, each graphene capillary has a size of 8×2 nm^2 (720 carbon atoms). First, the molecules inside left side box (Extended Data Fig. 10a) were relaxed in order to reach its equilibrium for 1 ns. Afterward, we applied a pressure of 0.9 bar on the vertical wall of the left box (shown by arrow in Extended Data Fig. 10a) to move the wall towards the capillary, so that water/ion molecules enter the capillary and flow towards the right box. The rate of filling of the capillary and the right box was found to depend significantly on the number of H_3O^+ and OH^- in the system (Extended Data Figs. 10b,c). We further found that after the equilibration, the concentration of ions inside the capillary is slightly lower than the concentration of ions in the system (left box) due to the higher water flow to the capillary. We have calculated the concentration of ions inside capillary with respect to the number of water molecules in it for different total concentration of ions in the system and studied its influence on the water flow rate through the capillary. We have found that by increasing the concentration of ions inside capillary, the water flow rate through the capillary decreases. When the ion concentration reaches > 6% (by number) the water flow rate significantly (~30 times) reduced (Extended Data Fig. 10d). This is qualitatively in agreement with the experimental estimation of ion concentration (see Methods section 'Influence of H_3O^+/OH^- ions') however the discrepancy in exact values can be expected because realistic GO channels contain functionalities, rough edges and so on, which are difficult to model accurately. It is noteworthy that the concentration of ions calculated in MD simulations for significant reduction of water flow rate, could be an overestimated value. The free space available in the interlayer channels of GO is <1 nm as used in MD simulations and, the functional

groups inside GO capillary may absorb ions, making the channel more hydrophilic. These effects were not included in MD simulations. Nevertheless, our MD simulations suggest that the dissociated water molecules inside the interlayer channels of GO membrane could significantly affect water permeation through the membrane.

The observed decrease in water flow rate with increasing ion concentration in the capillary could be due to ion hydration effects; with an increasing number of ions inside graphene capillary, water tends to remain inside the capillary thereby decreasing the water flow. Interestingly, a high concentration of dissociated water (~50%) was also observed at the interfaces and metallic surfaces and shows that they could be energetically stable even at room-temperature[54].

Interaction of H_3O^+/OH^- ions with water and graphene/GO capillary. First principles calculations were performed using Gaussian software and employing B3LYP/6-31g(d) level of theory to understand the interaction of H_3O^+ and OH^- ions with GO/graphene surface and, the surrounding water molecules. First, we optimized two GO flakes; each contains 62 carbon atoms, 22 hydrogen atoms, two epoxy and three hydroxyl groups. Then, we added 28 water molecules between them and re-optimized the system. The final configuration at this stage has shown the formation of few hydrogen bonds between confined water molecules and epoxy/hydroxyl functional groups. Later, we replaced two water molecules located at the center of two GO sheets by one H_3O^+ and one OH^- ion and re-optimized the system. It is evident from the resulted configuration (Fig. 4a) that H_3O^+ and OH^- ions form big clusters with the surrounding water molecules due to significant changes in the hydrogen bond network. Similar first principles calculations were also performed for H_3O^+ and OH^- ions in between two pristine graphene sheets and found the large hydrated cluster formation with surrounding water molecules (Fig. 4b). This additional calculation confirms that the chemistry of the capillary surface has no significant influence on the interaction of ions with water.

The first hydration shell of both H_3O^+ and OH^- ions (Figs. 4c,d) are found to be unique and form highly ordered hydrogen bonded water structure, in agreement with previous modelling[55]. In addition, ions form hydrogen bonds with epoxy/hydroxyl groups, if they are close to GO surface. However, the latter phenomenon is found to be less probable due to the presence of water molecules around H_3O^+/OH^- ions. Our first principles modelling clearly suggests that the experimentally observed reduction in water permeation in the presence of H_3O^+ and OH^- ions is due to their interaction with surrounding water molecules (via strong hydrogen bonds) which creates a large hydrated clusters, blocking the water transport. It is already reported that water diffusion coefficient significantly decreases in these large clusters of hydrated H_3O^+ ions[55]. In addition, the reaction dynamics of the creation/recombination of H_3O^+ and OH^- ions (eq. 4) in the presence of electric field could further contribute to the observed decrease in water permeation due to the perturbations caused in the hydrogen-bonded network of water inside graphene capillary[17]. Any disorder in the ordered hydrogen-bonded structure of water is also expected to affect the slip-enhanced flow of water through graphene capillary.

Influence of H_3O^+/OH^- ions. To study the influence of H_3O^+/OH^- ions on water permeation rate, we have carried out additional osmotic pressure driven water permeation experiments using GO membranes. These experiments were carried out using a similar experimental set-up shown in the Extended Data Fig. 7a, under same experimental conditions, but, by adding NaOH and HCl solutions of same concentration (to maintain same osmotic pressure) in both water and sucrose compartments. Here, the changes in water permeation rate were monitored with respect to pure water flux when the acid and base solution was absent. To eliminate complications in the following

discussion, we denote the solution added in water/sucrose compartments as S_w/S_s. Fig. 4e shows the water permeation rate for S_s and S_w of 10 mM concentration. When both S_s and S_w are 10 mM NaOH the water flux is increased to ≈ 0.15 L/h/m^2 with respect to a pure water flux of 0.1 L/h/m^2. However, it is decreased to ≈ 0.075 L/h/m^2 when S_s and S_w are 10 mM HCl. The small decrease/increase in the water flux in the case of HCl/NaOH could be attributed to the pH dependant decrease/increase in interlayer spacing of GO membranes[56]. However, the water flux is significantly reduced to ≈ 0.01 L/h/m^2 when 10 mM NaOH and 10 mM HCl as S_s and S_w, respectively. Fig. 4f further shows the decrease in the water permeation rate as the concentration increases from 1 mM to 10 mM, when S_s and S_w are NaOH and HCl, respectively. These experiments further confirm the demand for simultaneous presence of both H_3O^+ and OH^- ions in controlling the water permeation in GO membranes. Interestingly, the water permeation rate is recovered to the original value when the acid and alkaline solutions were substituted with pure water and sucrose solutions. As a control experiment, we have also performed measurements with one compartment is filled with 10mM NaOH or HCl while keeping the other compartment free from acid or base. No significant reduction in the water permeation rate was observed in this case. Similarly we have done experiments with $S_s=S_w=10$ mM NaCl and did not find any noticeable change in the water permeation rate.

Data availability. The data that support the findings of this study are available from the corresponding author upon reasonable request

31   Siegel, J., Lyutakov, O., Rybka, V., Kolská, Z. & Svorčík, V. Properties of gold nanostructures sputtered on glass. *Nanoscale Res. Lett.* **6**, 96 (2011).

32   Odwyer, J. J. Dielectric breakdown in solids. *Adv. Phys.* **7**, 349-394 (1958).

33   Kim, S. K. *et al.* Conductive graphitic channel in graphene oxide-based memristive devices. *Adv. Funct. Mater.* **26**, 7406-7414 (2016).

34   Eda, G. et al. Graphene oxide gate dielectric for graphene-based monolithic field effect transistors. Appl. Phys. Lett. 102, 133108 (2013).

35   Standley, B., Mendez, A., Schmidgall, E. & Bockrath, M. Graphene-graphite oxide field-effect transistors. *Nano Lett.* **12**, 1165-1169 (2012).

36   Lee, J. S., Lee, S. & Noh, T. W. Resistive switching phenomena: A review of statistical physics approaches. *Appl. Phys. Rev.* **2**, 031303 (2015).

37   Qin, S. *et al.* A physics/circuit-based switching model for carbon-based resistive memory with sp^2/sp^3 cluster conversion. *Nanoscale* **4**, 6658-6663 (2012).

38   Chen, C. *et al.* Annealing a graphene oxide film to produce a free standing high conductive graphene film. *Carbon* **50**, 659-667 (2012).

39   Borini, S. *et al.* Ultrafast Graphene Oxide Humidity Sensors. *ACS Nano* **7**, 11166-11173 (2013).

40   Pei, S. & Cheng, H. The reduction of graphene oxide. *Carbon* **50**, 3210-3228 (2012).

41   Park, S. et al. Colloidal suspensions of highly reduced graphene oxide in a wide variety of organic solvents. *Nano Lett.* **9**, 1593-1597 (2009).

42   Ganguly, A., Sharma, S., Papakonstantinou, P. & Hamilton, J. Probing the thermal deoxygenation of graphene oxide using high-resolution in situ X-ray-based spectroscopies. *J. Phys. Chem. C* **115**, 17009-17019 (2011).

43   Muller, R. A semiquantitative treatment of surface charges in DC circuits. *Am. J. Phys.* **80**, 782-788 (2012).

44   Jackson, J. D. *Classical Electrodynamics.* (John Wiley & Sons, 2007).

45   Geissler, P. L., Dellago, C., Chandler, D., Hutter, J. & Parrinello, M. Autoionization in liquid water. *Science* **291**, 2121-2124 (2001).

46   Mafe, S., Ramirez, P. & Alcaraz, A. Electric field-assisted proton transfer and water dissociation at the junction of a fixed-charge bipolar membrane. *Chem. Phys. Lett.* **294**, 406-412 (1998).

47   Pinkerton, T. D. *et al.* Electric field effects in ionization of water−ice layers on platinum. *Langmuir* **15**, 851-856 (1999).

48   Wilson, N. R. *et al.* Graphene oxide: structural analysis and application as a highly transparent support for electron microscopy. *ACS Nano* **3**, 2547–2556 (2009).

49   Loh, K. P., Bao, Q., Eda, G. & Chhowalla, M. Graphene oxide as a chemically tunable platform for optical applications. *Nat. Chem.* **2**, 1015–1024 (2010).

50   Plimpton, S. Fast parallel algorithms for short-range molecular dynamics. *J. Comput. Phys.* **117**, 1-19 (1995).

51   Vacha, R., Buch, V., Milet, A., Devlin, J. P. & Jungwirth, P. Autoionization at the surface of neat water: is the top layer pH neutral, basic, or acidic? *Phys. Chem. Chem. Phys.* **9**, 4736-4747 (2007).

52   Vacha, R., Horinek, D., Berkowitz, M. L. & Jungwirth, P. Hydronium and hydroxide at the interface between water and hydrophobic media. *Phys. Chem. Chem. Phys.* **10**, 4975-4980 (2008).

53   Mills, R. Self-diffusion in normal and heavy water in the range 1-45.deg. *J. Phys. Chem.* **77**, 685-688 (1973).

54   Meyer, B. *et al.* Partial dissociation of water leads to stable superstructures on the surface of zinc oxide. *Angew. Chem. Int. Ed.* **43**, 6641-6645 (2004).

55   Elena, B., Alexander, P. L. & Aatto. L. Investigation of water clusters containing OH$^-$ and H$_3$O$^+$ ions in atmospheric conditions. A molecular dynamics simulation study. *J. Phys. Chem. B* 106, 6479−6487 (2002).

56   Huang, H. et al. Salt concentration, pH and pressure controlled separation of small molecules through lamellar graphene oxide membranes. *Chem. Commun.* **49**, 5963-5965 (2013).
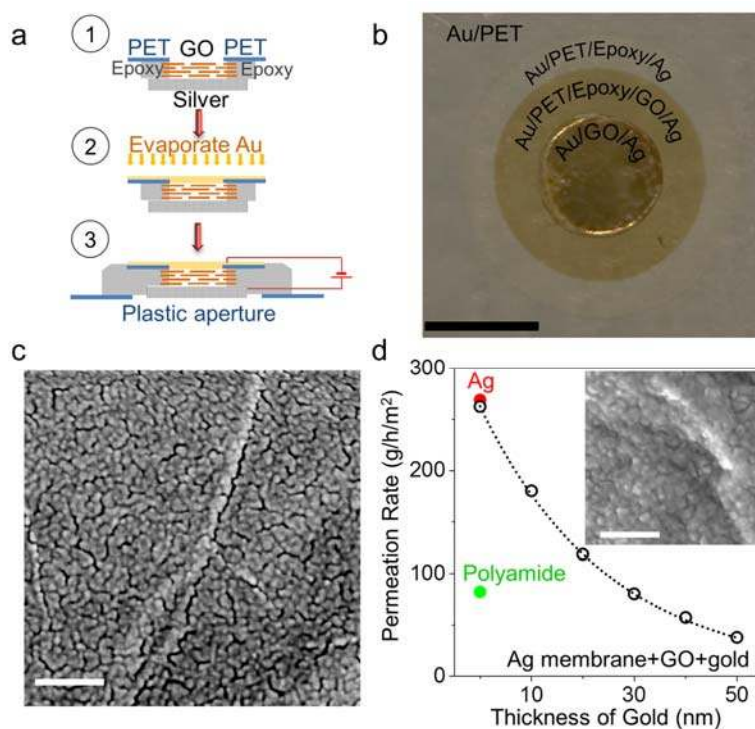
Extended Data Figure 1| Metal-GO-metal sandwiched membranes. a, Fabrication procedure for the metal-GO-metal sandwich membrane. **b,** Photograph of one of our metal-GO-metal sandwich membranes attached to the PET sheet (step 2 in **a**). Scale bar: 6 mm. This was further attached onto another plastic disc for sealing the metal container for gravimetric testing. **c,** SEM image showing the discontinuities and voids in a 10 nm gold thin film on GO membrane. Scale bar: 150 nm. **d,** Water permeation rate of metal-GO-metal sandwiched membranes as a function of gold electrode thickness. The dotted line is guide to the eye. Water permeation rates of bare porous silver (Ag) support (red color filled circle), and commercial polyamide nanofiltration membrane (green color filled circle) are provided for the comparison. Inset, SEM image of 50 nm thick gold thin film on GO membrane. Scale bar: 150 nm.
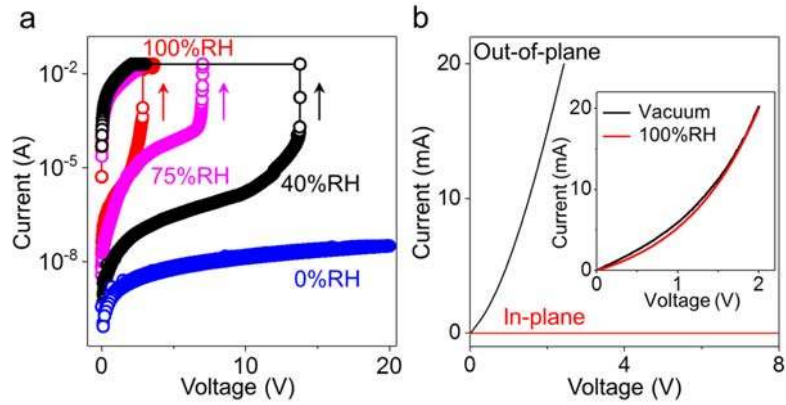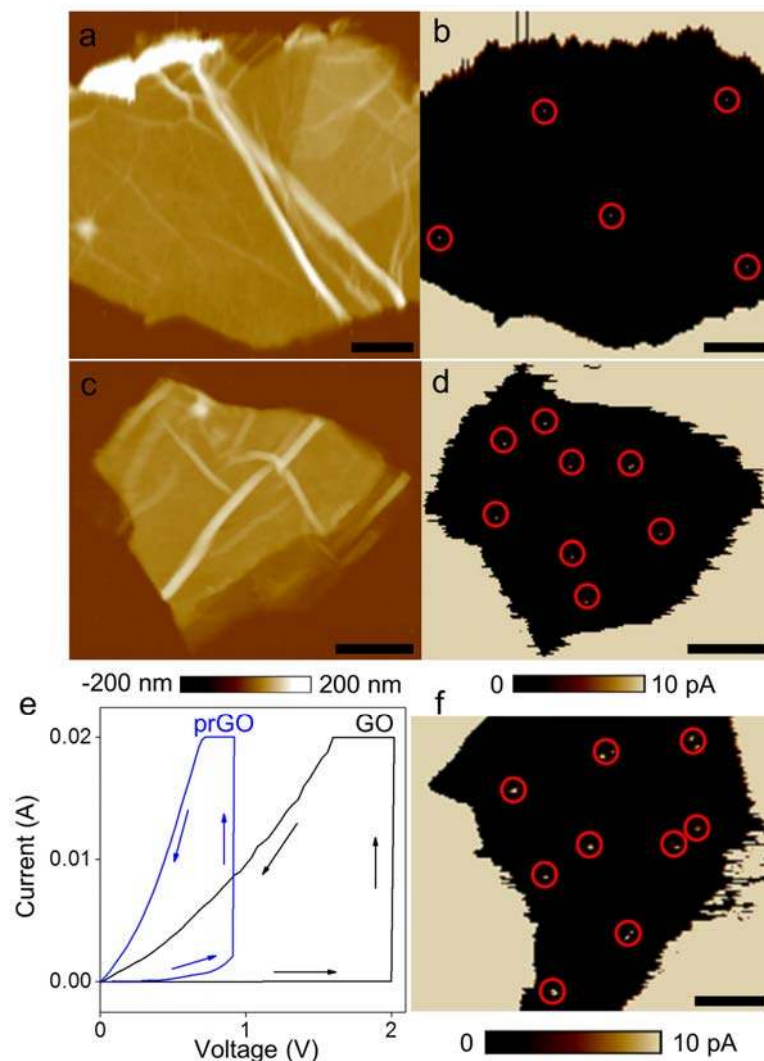
Extended Data Figure 2| Conducting filament formation in GO membrane and its electrical characterization. a, *I-V* characteristics during the first voltage sweep showing a sudden increase in the current for membranes exposed to humid conditions suggesting partial electrical breakdown of GO membrane and conducting filament formation. **b,** In-plane and out-of-plane *I-V* characteristics of the GO membrane after the filament formation. Inset: Out-of-plane *I-V* characteristics of GO membrane at 100% RH and vacuum.
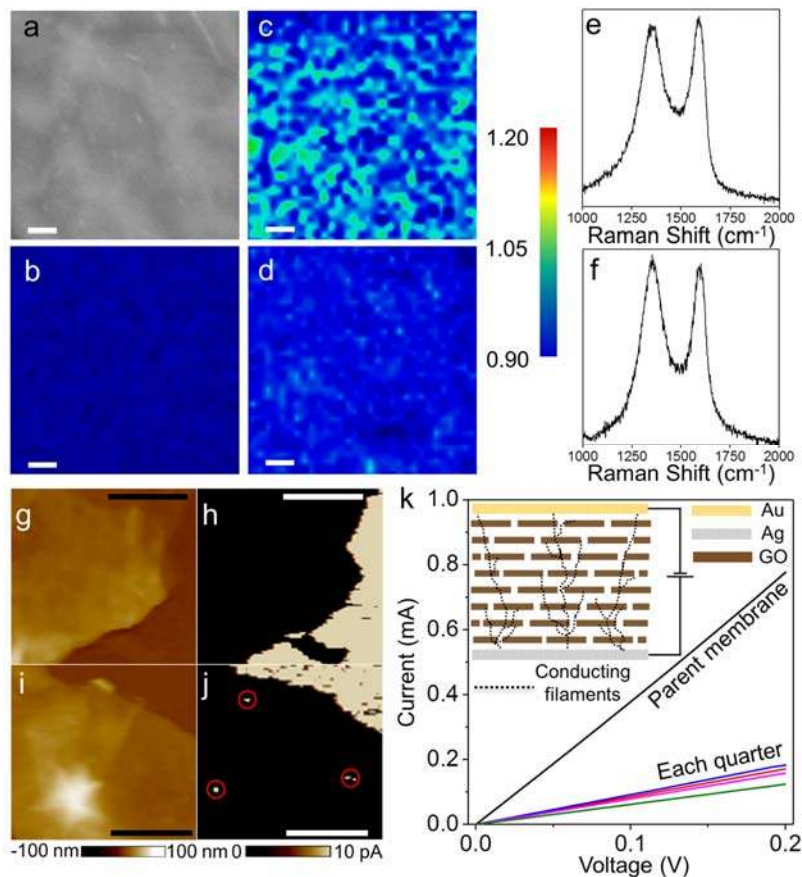
Extended Data Figure 3| Raman and AFM characterization of conducting filaments in GO membrane. a, Topographical SEM image of a GO membrane after the formation of conducting

filaments. Raman intensity ratio (I_D/I_G) mapping of D and G bands for **b**, a pristine GO membrane and **c** and **d**, a GO membrane after conducting filaments had been formed. (**c**) Raman imaging from the membrane surface close to the positive electrode (~ 200 nm away). **d**, Raman imaging from the membrane surface close to the negative electrode (~100 nm away). **e** and **f**, show the Raman spectra from the dark blue and green colored regions in **c**, respectively. Topography and the corresponding TUNA current image of pristine GO (**g** and **h**) and conducting GO (**i** and **j**) membranes (filament formed at 100% RH) exfoliated on a gold thin film coated Si substrate. The conducting filaments are marked by red circles. All the scale bars represent 1 μm. **k,** Out-of-plane *I-V* characteristics of a conducting GO membrane with a diameter of ~7 mm before (parent membrane) and after dividing into four equal pieces. Inset: Schematic of the structure of conducting carbon filaments in the GO membrane.


Extended Data Figure 4| Influence of intercalated water and oxygen content on conducting filament formation in GO membrane. Topography (left) and the corresponding TUNA current images (right) of GO membranes after the filament formation at 40% RH (**a** and **b**) and inside liquid water (**c** and **d**). **e,** *I-V* characteristics of pristine and partially reduced GO membranes during

the first voltage sweep at 100% RH showing partial breakdown. **f,** TUNA current image of partially reduced GO membrane after filament formation. The conducting filaments are marked by red circles. Scale bars represent 2 μm.
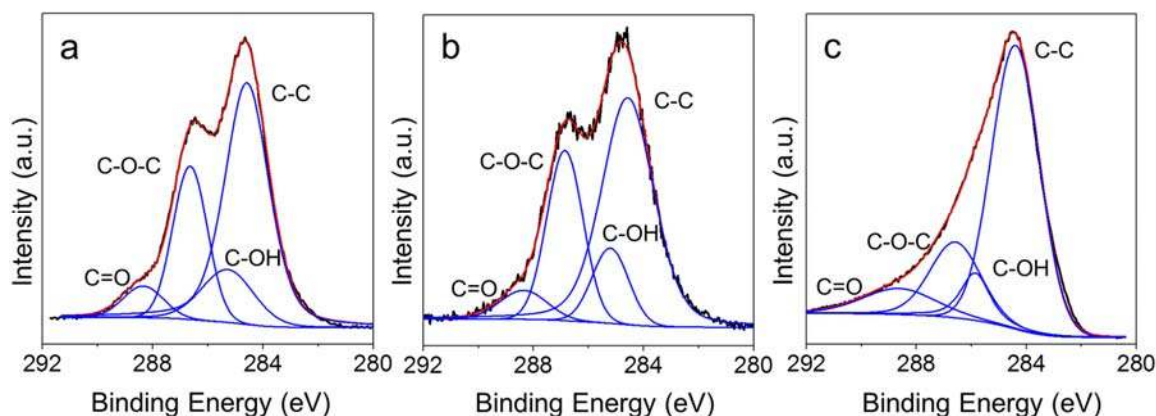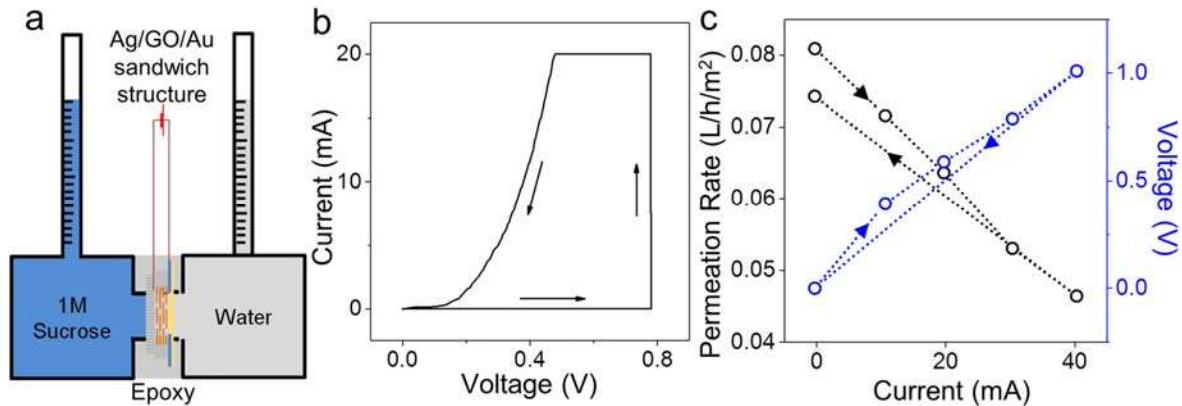

Extended Data Figure 5| XPS characterization of GO membranes. a, C 1s spectrum from a pristine GO membrane. **b** and **c,** C 1s spectrum from GO membranes used for the electrically controlled permeation experiments after filament formation. **b,** shows a spectrum from a freshly cleaved membrane surface close to the inner middle region and **c,** is from a freshly cleaved surface close to the positive electrode. Black lines: raw data; red lines: the fitting envelope; blue lines: deconvolved peaks attributed to the chemical environments indicated.
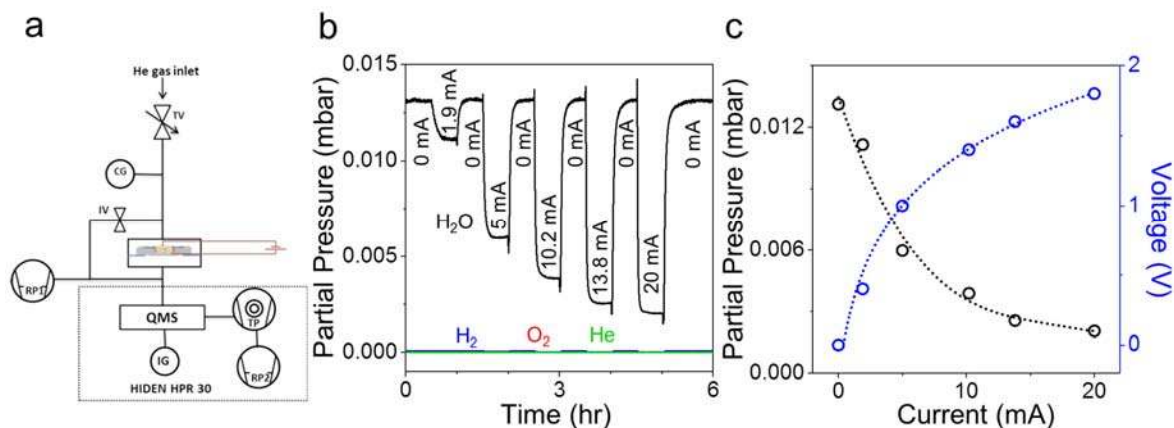

Extended Data Figure 6| Mass spectrometry for probing electrically controlled water permeation. a, Schematic of the experimental setup for mass spectrometry (MS) measurements. A throttle valve (TV) controls the gas inlet with a capacitance gauge (CG) used to measure the upstream pressure. An isolation valve (IV) isolates upstream and downstream sides of the membrane. A rotary pump (RP1) evacuates the feed as well as the permeate side to 1 mbar. The quadrupole mass spectrometer (QMS) measures the downstream partial pressure. A turbomolecular pump (TP) backed by a rotary pump (RP2) evacuates the high vacuum chamber of the mass spectrometer. An active ion gauge (IG) measures the pressure down to 1×10^{-9} Torr in the high vacuum side. **b,** The partial pressure of He, H_2, O_2 and H_2O at the permeate side as a

function of time at different current through the membrane. No detectable change is observed in the partial pressure values of He, H_2 and O_2 under different current through the membrane. **c,** The partial pressure of H_2O as a function of the current across the GO membrane, and the corresponding *I-V* characteristics (color-coded axis). The dotted lines are guide to the eye.


Extended Data Figure 7| Electrically controlled liquid water permeation in GO membranes. a, Schematic illustrating the experimental set-up. **b,** *I-V* characteristics of Au/GO/Ag membrane during the first voltage sweep while it is immersed in liquid water in the experimental set-up. **c,** Liquid water permeation rate as a function of current across the membrane after the filament formation, and the corresponding *I-V* characteristics (colour coded axis). Sample to sample variations in the permeation is <30% (total three samples measured).
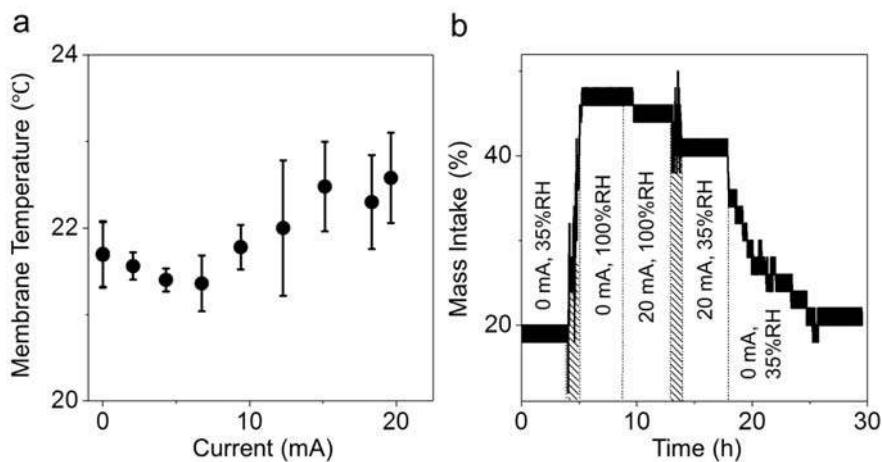
Extended Data Figure 8| *In-situ* **membrane temperature and water absorption measurements. a,** Measured membrane temperature as a function of the current flowing across the membrane during the electrically controlled water permeation experiment. Error bars, standard deviation from 10 different measurements across the sample. **b,** The weight intake of a Au/GO/Ag membrane (1 μm thick GO) at different humidity and at different electric current values. Weight intake is calculated with respect to the weight of the membrane at 0% RH. The shaded areas show time during humidity sweeps.
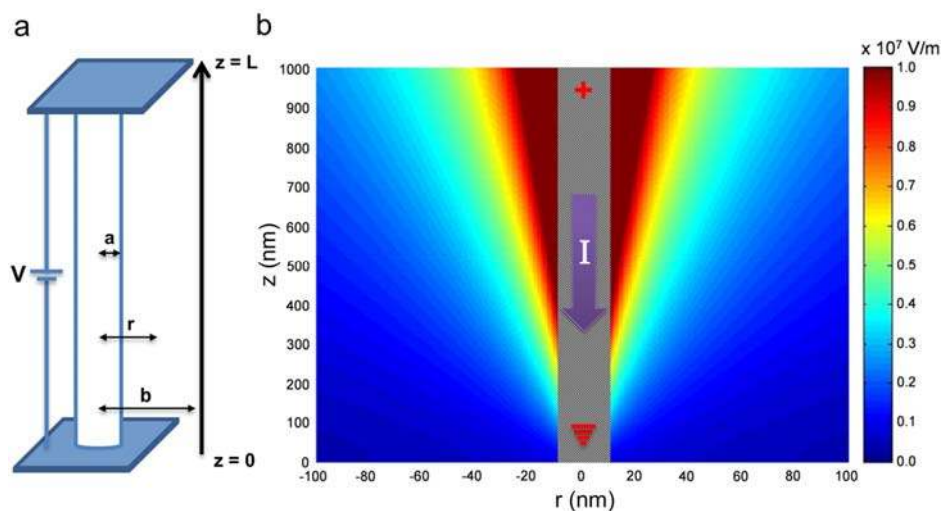
Extended Data Figure 9| Electric field around a current carrying conductor. a, Schematic showing the application of a voltage *V* across an electrically conducting wire with radius *a* and length *L*. *b* is a point at which the potential decays to zero. *r* represents any point between *a* and *b* where the electric field, *E*, is calculated. **b,** Magnitude of *E* and its spatial distribution as a function of *r* and *z* around a conductive filament with 1 V potential difference across the ends and with 1 nA current flow.
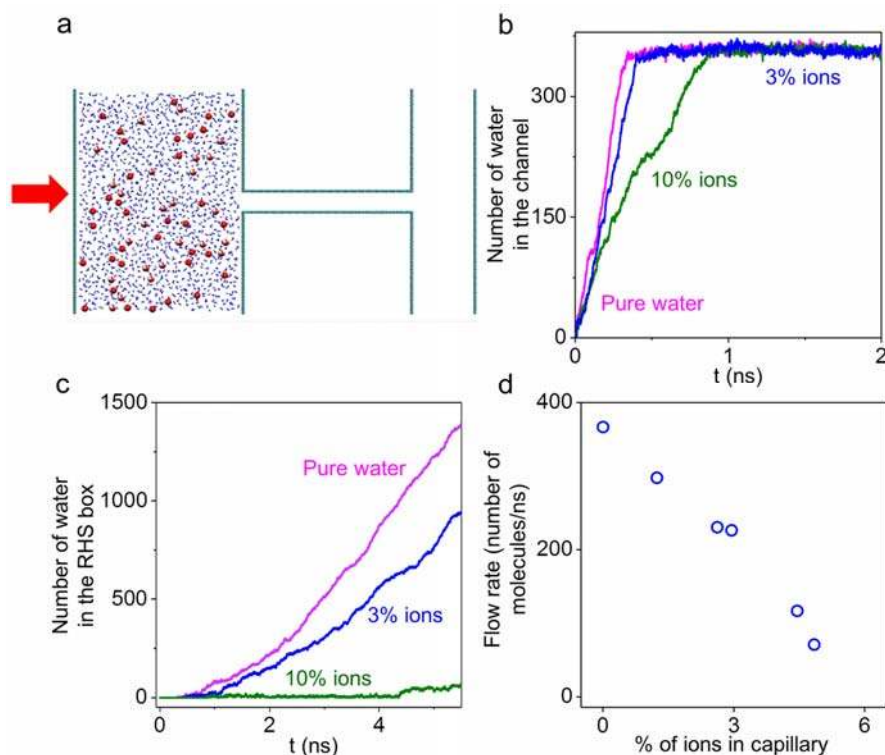
Extended Data Figure 10| Molecular dynamics simulations. a, Side view of our MD simulation set-up used to study the flow of water mixed with H_3O^+ and OH^- ions in the graphene capillary. The model contains two boxes which are connected by a graphene capillary. At the beginning of

the simulation, water was mixed with H_3O^+ and OH^- (red and white dots) ions. By moving the left wall (subjected to external pressure) of the box towards the capillary, the water flow is created and the right box is gradually filled. The arrow indicates the direction of the applied external pressure on the left wall of the box. **b**, Number of water molecules in the capillary and **c**, number of water molecules in the right box for the pure water and water with ions once pressure is applied to the left box (colour coded label). **d**, Water flow rate as a function of concentration of ion inside the capillary.